Computers and Geosciences 119 (2018) 49–67

Contents lists available at ScienceDirect

Computers and Geosciences

journal homepage: www.elsevier.com/locate/cageo

Research paper

Multi-objective unstructured triangular mesh generation for use in hydrological and land surface models

Christopher B. Marsh[a,b,*], Raymond J. Spiteri[a,c], John W. Pomeroy[a,b], Howard S. Wheater[a,b]

[a] Center for Hydrology, Dept. Geography, University of Saskatchewan, Canada
[b] Global Institute for Water Security (GIWS), University of Saskatchewan, Canada
[c] Numerical Simulation Lab, Dept. Computer Science, University of Saskatchewan, Canada

ARTICLE INFO

Keywords:
Hydrology
Mesh generation
Modelling
Unstructured grid
Multi-objective refinement

ABSTRACT

Unstructured triangular meshes are an efficient and effective landscape representation that are suitable for use in distributed hydrological and land surface models. Their variable spatial resolution provides similar spatial performance to high-resolution structured grids while using only a fraction of the number of elements. Many existing triangulation methods either sacrifice triangle quality to introduce variable resolution or maintain well-formed uniform meshes at the expense of variable triangle resolution. They are also generally constructed to only fulfil topographic constraints. However, distributed hydrological and land surface models require triangles of varying resolution to provide landscape representations that accurately represent the spatial heterogeneity of driving meteorology, physical parameters and process operation in the simulation domain. As such, mesh generators need to constrain the unstructured mesh to not only topography but to other important surface and sub-surface features. This work presents novel multi-objective unstructured mesh generation software that allows mesh generation to be constrained to an arbitrary number of important features while maintaining a variable spatial resolution. Triangle quality is supported as well as a smooth gradation from small to large triangles. Including these additional constraints results in a better representation of spatial heterogeneity than from classic topography-only constraints.

1. Introduction

Distributed hydrological and land surface models aggregate the surface and sub-surface into internally homogenous control volumes (Vrugt et al., 2008). These control volumes are used to discretize the mass and energy conservation equations or to apply point-scale models. Correct selection of these control volumes has profound implications for the numerical stability of the discretized equations (Berger and Colella, 1989; Hagen et al., 2000; Parrish and Hagen, 2007; Caviedes-Voullième et al., 2012). Cold regions are characterized by seasonal snowcover and snowfall; here, snow-landscape interactions and energy flux considerations further complicate the selection of control volumes. In these regions, landscape heterogeneity such as vegetation, slope, aspect, and elevation are often critical controls on important processes such as blowing snow (Pomeroy et al., 1997; Essery et al., 1999; Mott et al., 2008), vegetation interactions (Pomeroy et al., 1998; Gelfan et al., 2004; Ménard et al., 2014), snowmelt (Essery and Pomeroy, 2004; Dornes et al., 2008a; Grünewald et al., 2010; Marsh et al., 2012; Debeer and Pomeroy, 2017), and runoff dynamics (Carey and Woo, 2001). Surface heterogeneity is also critical for land-atmosphere interactions (Foken, 2008; Husain et al., 2016). The commonly used fixed-resolution control volume, e.g., raster approach, often has substantial computation burdens (Vivoni et al., 2004; Caviedes-Voullième et al., 2012), as well as high uncertainty when applied to areas of interest for water resources such as mountain watersheds. There is a motivation for a discretization that balances surface heterogeneity, numerical requirements, and a reduction in computational elements for use with hydrological and land-surface models.

Triangular meshes represent the topography via a set of irregularly sized, non-overlapping connected triangles (Chang, 2008). Meshes with variable sized and shaped elements are *unstructured*. Areas of high spatial variability can have a greater density of small triangles than areas that are more homogeneous, providing a more efficient terrain representation than the raster format (Shewchuk, 1996) by reducing computational elements in models by up to 90% (Ivanov et al., 2004). Efficiency increases of this magnitude make distributed modelling approaches more feasible and less uncertain due to reduced parameter sets, initial conditions, and wall-clock time (e.g., Ivanov et al., 2004; Kumar et al., 2009a,b). Due to the widespread availability of raster data, unstructured meshes for hydrology are typically derived from raster digital elevation

---

[*] Corresponding author. Center for Hydrology, Dept. Geography, University of Saskatchewan, Canada.
E-mail address: chris.marsh@usask.ca (C.B. Marsh).

https://doi.org/10.1016/j.cageo.2018.06.009
Received 12 September 2017; Received in revised form 30 April 2018; Accepted 25 June 2018

models (DEMs). Because these meshes act as an approximation to landscape variability, care must be taken during creation, and constraints on triangle shape, size, and error to the underlying raster(s) should be included to ensure suitability for hydrological modelling (Caviedes-Voullième et al., 2012; Bilskie and Hagen, 2013).

Two common methods for mesh creation exist: point selection and domain constraints. There are five popular selection algorithms: Heuristic, Hierarchy, Skeleton, and Filter (also known as Very Important Points, VIP) (Lee, 1991; El-Shimy et al., 2005; Chang, 2008), and ArcGIS tools. These share the trait that possible stopping criteria be either a pre-set number of points to be selected or pre-set differences in elevation between the selected point and neighbouring raster cells (Lee, 1991). Importantly, these methods make no guarantees concerning triangle quality. Therefore, long skinny triangles can be created with poor gradations from small to large triangles. These triangles are generally unsuitable for use as a discretization mesh in numerical applications. An example of poor point selection is shown in Fig. 1, where the selected points (green dots) duplicate the structured mesh corners, doubling the number of elements (black lines are triangle edges). In areas of generally flat topography, such as plains or broad valley bottoms, constraining meshes only to topography fails to capture the spatial heterogeneity of hydrologically important characteristics. Alternatively, inner and outer domain boundaries such as basin delineation, streams, and lakes are defined and triangles are inserted to cover the area defined by these boundaries. Triangular mesh generation using this technique is generally done via constrained Delaunay triangulation (Ruppert, 1995; Shewchuk, 2002). Strong guarantees on triangle shape and inner angles ensures suitability for use as a discretization mesh for numerical applications.

In this paper, a multi-objective meshing tool, *Mesher*, is presented. Based on an existing, high-quality implementation of constrained Delaunay triangulation, its novel contribution is in how triangles are chosen for refining. Mesher uses various objective functions to measure triangle error with the underlying primary raster as well as constraining to non-topographic discrete and classified data (e.g., land cover, soils). This permits variably sized triangles throughout the domain, allows for guarantees about triangle quality and shape, and ensures that spatial heterogeneity in secondary features is represented. Specifically, this meshing software is optimized for use in hydrological and land surface models that mix many point-scale and non-PDE (partial differential equation) distributed algorithms along with PDE discretizations. Due to this mixing of methods, meshes are generated considering only the landscape, e.g., elevation, vegetation, and soil, and not the discretization of physical processes such as Hagen et al. (2002) or Parrish and Hagen (2007) who consider numerical error in the mesh generation. This meshing tool is quantitatively tested against an existing mesh generation method, and a surface heterogeneity measure is used to quantify whether important landscape characteristics are well approximated.

2. Meshing algorithm

2.1. Overview

The core meshing algorithm is built upon the constrained Delaunay meshing algorithm of J. Shewchuk (2002), as implemented in the Computational Geometry Algorithms Library (CGAL; Rineau (2016)). In brief, Delaunay meshes constrain triangle inner angles, edge lengths, number of total triangles, and the gradation from small to large triangles in the domain (Shewchuk, 2002). Delaunay meshes have been used with success for a coupled representation of surface-sub-surface processes (Qu and Duffy, 2007) and for shallow water flow equations (Hagen et al., 2001, 2002; Kumar et al., 2009a). Due to the importance of including sub-mesh scale vertical features (Bilskie et al., 2015) as well representing rivers and streams, these constraint features may be included. Boundary and inner feature constraints are defined via planar straight-line graphs (PSLGs). The pre- and post-processing steps, as well as the multi-objective refinement algorithm, are detailed below.

2.2. Details

Outlined in Algorithm 1, the meshing algorithm uses the extent of the DEM to bound the meshing area. All optional secondary input parameters (e.g., vegetation and soils) are converted to the DEM's coordinate system and are clipped to the DEM's spatial extent, allowing mismatched raster resolutions and extents in these data. The data/nodata region of the DEM is used to generate an (optionally simplified) outer PSLG. The *z*-value of the triangle vertices (v_z) are assigned a value from the DEM. However if the PSLG is simplified it may result in a vertex laying outside the original raster extent. These invalid vertices have their *z*-value interpolated from neighbour vertices. More novel DEM to mesh interpolation techniques such as Bilskie and Hagen (2013) could be included if required. These pre-processing steps are done in Python. The core meshing algorithm is written in C++11. All geospatial manipulation is done via the Geospatial Data Abstraction Library(GDAL) (GDAL Development Team, 2016).

```
input  : A digital elevation map DEM
input  : An optional set of secondary constraints parameters P

Extent ← Extent(DEM)
nodata ← NoDataValue(DEM)
Projection ← GetProjection(DEM)
foreach p in P do
    ClipExtent(p, Extent)
    NoDataValue(p)← nodata
    Project(p, Projection)
end
PSLG ← Polygonize(DEM)
mesh ← Mesher(PSLG, DEM, P)
foreach v in Mesh verticies do
    if v outside Extent then
        Interpolate $v_z$ from connected verticies
    end
end
```

Algorithm 1. High-level outline of the pre- and post-processing steps.

The Delaunay algorithm inserts triangles that fill the PSLG region. Each candidate triangle that is generated may either be accepted or rejected for further refinement; this is outlined at a high-level in the *IsBad* function in Algorithm 2. Further refinement of a triangle may be required if the triangle's total area is above a threshold, if it poorly represents the underlying raster, or if it has inner angles that are below a threshold (skinny triangles). This refinement strategy enforces a rigorous application of supplied tolerances. A minimum area constraint is used to stop the meshing algorithm from over-refining a triangle. If triangles are to be produced at a similar resolution as the input DEM, an iterative smoothing can be applied to the input DEM to reduce stair stepping in the output mesh.

```
input    : A set of rasters $R$, at least 1 topographic raster
input    : A candidate triangle produced by the CGAL meshing
           algorithm $tri$
input    : Maximum allowed error between triangle and raster $tol$
optional: An optional set of categorical constraints $C$
optional: Maximum category mode constraint $cat\_tol$
optional: Maximum area $maxarea$
optional: Minimum area $minarea$

Function IsBad (tri)
    if inner angle $< 22.5$ then return true ;
    if tri area $>$ maxarea then return true ;
    if tri area $<=$ minarea then return false ;
    foreach $r$ in $R$ do
        if ErrorMetric(tri) $> t$ then return true;
    end
    foreach $c$ in $C$ do
        if Mode(tri) $< ct$ then return true;
    end
    return false
Function ErrorMetric (tri)
    $v_0, v_1, v_2 \leftarrow$ triangle vertexes
    bbox $\leftarrow$ bounding box of $v_0, v_1, v_2$
    if bbox extent $>$ DEM extent then
        bbox $\leftarrow$ Clipbbox
    end
    rtri $\leftarrow$ GDALRasterizeGeometries(tri, bbox)
    foreach Cell in rtri do
        if Cell in triangle then
            Pred $\leftarrow$ Predicted value from plane equation
            Error $\leftarrow$ Accumulate difference $Cell - Pred$ as required
        end
    end
    return Error
```

Algorithm 2. High-level description of the rejection/acceptance algorithm.

An example of a candidate triangle is shown in Fig. 2. Overlain on the elevation raster (coloured; red = high, blue = low) is the in-construction unstructured mesh (black lines). The triangle has been rasterized and the bounding box to this triangle is shown by the extent of the black area. Cells touched by the triangle within this bounding box are shown in grey and those untouched are shown in black. The cells in this mask exactly correspond to cells in the underlying raster. Using a plane interpolant defined by this triangle, in combination with the rasterized binary triangle mask, an error metric between the underlying raster and the triangle can be computed. Multiple error metrics were used: Root Mean Square Error (RMSE), maximum difference, and difference in mean value. All error metrics (E) are compared to some threshold (ε; $E < \varepsilon$). RMSE is given as

$$RMSE = \sqrt{\frac{\sum_{i=1}^{n}(z_o(x_i, y_i) - f(x_i, y_i))^2}{n}} \tag{1}$$

and is computed between the plane interpolant $f(x, y)$ and the raster cell value $z_o(x, y)$ for n non-masked cells, i.e., the grey cells in Fig. 2, given by normalized coordinates (x, y). Maximum difference (herein tolerance *Tol*) is given as the maximum of the set of differences between the plane interpolant ($f(x, y)$) and raster ($z_o(x, y)$) values for non-masked cells. Numerically, this is given as

$$Tol = \max_{i \in \{1,2,\ldots,n\}}(\{|z_o(x_i, y_i) - f(x_i, y_i)|\}). \tag{2}$$

Mean difference (MD) is given as:

$$MD = \left| \frac{\sum_{i=1}^{n} z_o(x_i, y_i)}{n} - \frac{z_0 + z_1 + z_2}{3} \right|, \tag{3}$$

where z_0, z_1, z_2 are the three z-coordinates of the triangle vertices and $z_o(x, y)$ are the n non-masked raster cells. Effectively, this computes the difference of the mean of each triangle vertex and the mean of all the non-masked raster cells.

A triangle may be further constrained to any arbitrary set of continuous

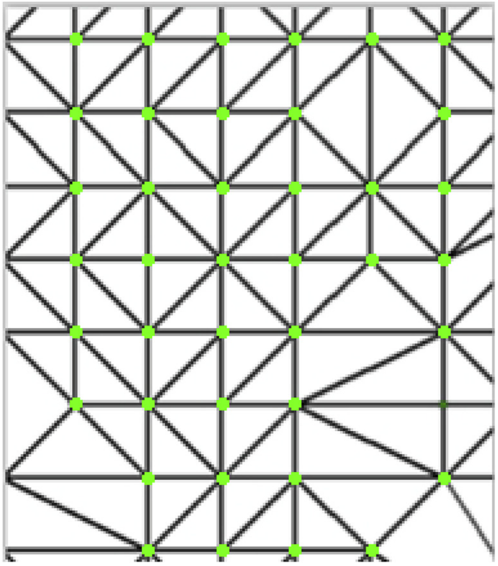

Fig. 1. Example of poor mesh generation from a raster. Raster cells have been cut in half, doubling the number of computational elements in places. Triangle edges are in black.

or classified data. (e.g., vegetation, soils). For classified data, the dominant feature class in this triangle is checked for exceeding a coverage threshold; e.g., 70% of a cell is covered by a single vegetation class. For discrete constraints, the above-described error metrics may be used.

Alternatively, a more generic weighted approach is also possible. Each input raster constraint is assigned a weight w_r such that $\sum_{r=1}^{R} w_r = 1$, and a total weight tolerance to exceed is specified. This is a not a completely rigorous approach; however, it allows for prioritizing various constraints over others. This algorithm is detailed in Algorithm 3. In contrast to the rigorous tolerance checking detailed above, where failing to meet any raster constraint results in refinement, the weighting approach checks each raster tolerance before determining acceptance of the triangle. The total triangle weighted quality threshold W is given as

$$W = \sum_{r=1}^{R} \alpha_r w_r, \tag{4}$$

where w_r is the raster weight for each raster r of the total set of raster constraints R. The term α_r is set as follows: $\alpha_r = 1$ when the triangle meets that raster constraints tolerance, and $\alpha_r = 0$ when it does not. This requires a certain number of constraints are met before accepting the triangle. Small-angled triangles and triangles larger than the specific maximum area are unconditionally rejected and triangles at or below the specified minimum area are unconditionally accepted as they cannot be refined further.

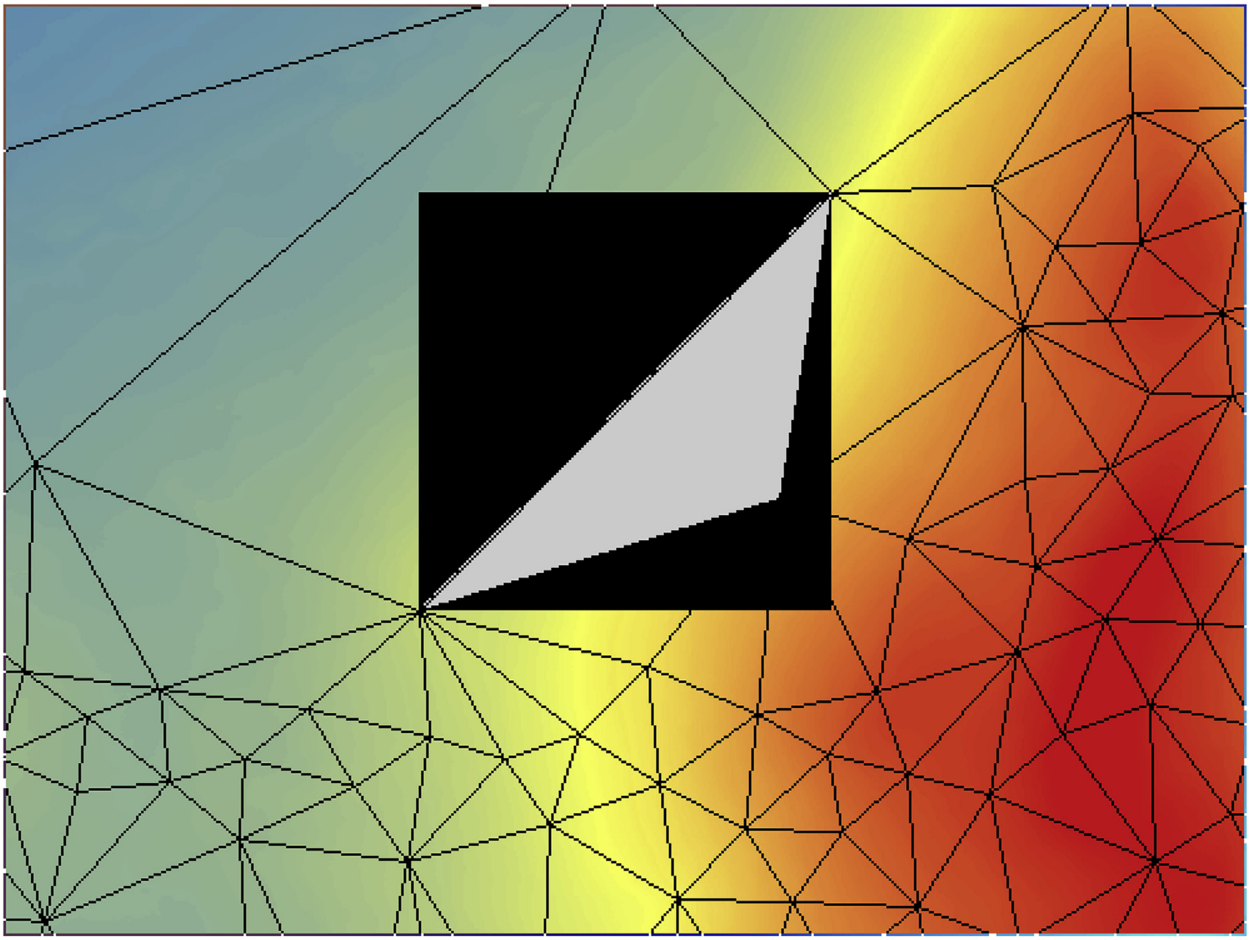

Fig. 2. Elevation raster (colour; red = high, blue = low) overlain by in-construction unstructured mesh (black lines). Candidate rasterized triangle shown centre. Black shows raster cells not touched by the triangle, grey for those that are. This is used in determining error between triangle and underlying raster. (For interpretation of the references to colour in this figure legend, the reader is referred to the Web version of this article.)

```
input    : A set of rasters $R$, at least 1 topographic raster
input    : A candidate triangle produced by the CGAL meshing
           algorithm $tri$
input    : Maximum allowed error between triangle and raster $tol$
input    : Weight tolerance to exceed to accept $tolweight$
optional: An optional set of categorical constraints $C$
optional: Maximum category mode constraint $cat\_tol$
optional: Maximum area $maxarea$
optional: Minimum area $minarea$
optional: Weights for each raster $weights$
optional: Total weight for this triangle $totalweight$
optional: Weight given to a raster $w$

Function IsBad_weighted (tri)
    totalweight =0
    if inner angle $<$ 22.5 then  return true ;
    if tri area $>$ maxarea then  return true ;
    if tri area $<=$ minarea then  return false ;
    foreach $r$ in $R$ do
        if ErrorMetric($tri$) $> t$ then totalweight += $w$;
    end
    foreach $c$ in $C$ do
        if Mode($tri$) $< ct$ then totalweight += $w$;
    end
    if totalweight $>$ tolweight then  return false ;
    return true
Function ErrorMetric (tri)
    $v_0, v_1, v_2 \leftarrow$ triangle vertexes
    bbox $\leftarrow$ bounding box of $v_0, v_1, v_2$
    if bbox extent $>$ DEM extent then
        bbox $\leftarrow$ Clipbbox
    end
    rtri $\leftarrow$ GDALRasterizeGeometries(tri, bbox)
    foreach Cell in rtri do
        if Cell in triangle then
            Pred $\leftarrow$ Predicted value from plane equation
            Error $\leftarrow$ Accumulate difference $Cell - Pred$ as required
        end
    end
    return Error
```

Algorithm 3. Instead of rigorously ensuring each tolerance is met, a weighted approach is possible. This allows giving priority to various input constraints. For this approach, a weight (w_r) is specified for each constraint raster, where $\sum_{r=1}^{R} \alpha_r w_r = 1$. Each raster is evaluated for fulfilling the corresponding tolerance, and success or failure is weighted by the raster weight. A final weighted quality threshold must be exceeded to accept the triangle.

The mesh generation outlined herein has been designed to address a gap in mesh generation for hydrological and land-surface numerical models that combine various types of process representation, such as point scale, distributed, and PDE discretized equations. These models are commonly applied to large spatial extents and to cold regions where dominate processes change during the year. It is therefore difficult to optimize the mesh using either error truncation analysis or *a posteriori* metrics for a single process. However, *a posteriori* refinement such as John (2000); Verfürth (2005) could be integrated into the triangle selection/rejection routine. Inclusion of truncation error in the mesh generation has been shown to improve results and decrease computational burden (Parrish and Hagen, 2007). Two examples of this algorithm (rigorous variant) in progress are shown in Figs. 3 and 4. In Fig. 3, an idealized Gaussian hill has been meshed. Each panel shows an iteration of the meshing algorithm, and the triangles are coloured with the RMSE of the triangles. For the first iteration, PLGS filling triangles are inserted. However, the error of each triangle is large, and so the triangles are rejected and further refined. Due to the conic shape of the hill, that lies on a flat plane, the outer triangles converge quickly. As the meshing continues, increasingly small triangles are inserted near the peak of the hill to capture the sharp curvature. At the final iteration, the triangle tolerance has been met and the algorithm terminates. In Fig. 4, a domain meshed using an elevation and vegetation constraint (expanded in detail in Section 3; shown in Fig. 8) is shown at various stages of completion. The triangle faces are coloured based upon one of: triangle is ok, has failed elevation tolerance, has failed vegetation tolerance, or has failed both. Due to the large sizes of the initial two triangles, a single vegetation class is sufficiently dominating to pass the vegetation tolerance. However, elevation fails. As the mesh is refined,

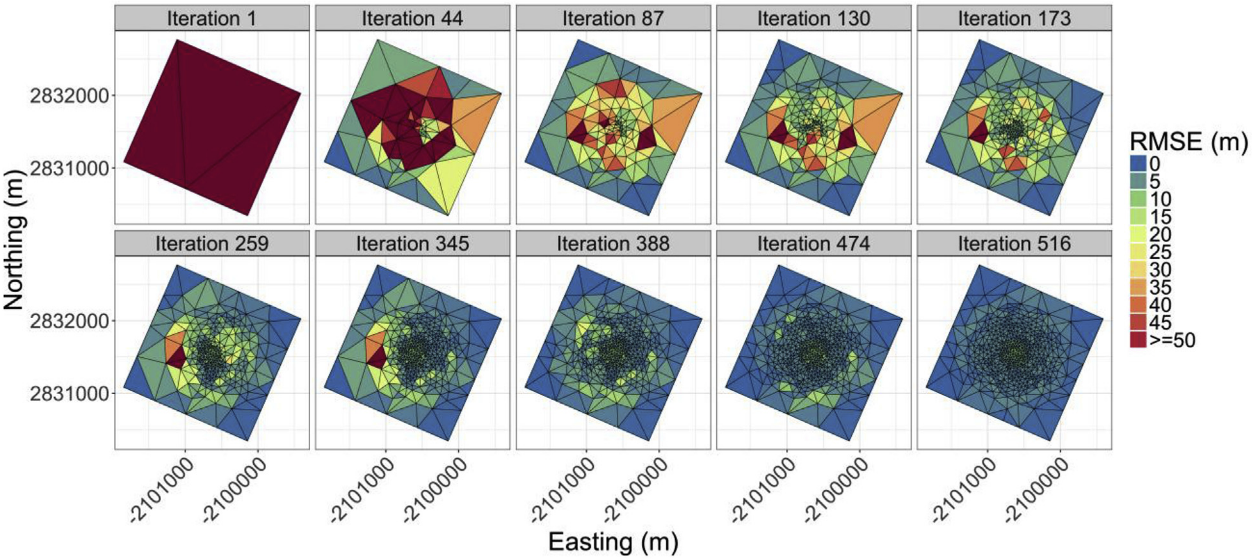

Fig. 3. Output from the meshing algorithm at various stages of refinement for an idealized Gaussian Hill that lies on a flat plane. The triangulation is optimizing only on elevation RMSE. Initially three PLSG filling triangles are inserted into the domain. Due to the high RMSE, these are rejected, and small triangles are inserted into the domain. As the meshing continues, increasingly small triangles are inserted near the peak of the hill to capture the sharp gradients. At the end, the triangle tolerance has been met and the algorithm terminates.

triangles begin to pass the elevation tolerance but now fail the vegetation tolerance. By iteration 869, there are triangles on the right-hand side of the domain located in an area of patchy vegetation that still require refinement. Because these triangles have been refined to the minimum triangle size, they are unconditionally accepted. Although many iterations are required, fewer and fewer triangles are refined in each iteration, resulting in fast convergence.

After generation of the mesh, a post-processing Lloyd optimization (Tournois et al., 2010) step can be performed that relaxes the mesh further improve gradation from small to large triangles. This step does negate the guarantees of the rigorous tolerance checking because triangle geometry is changed. Once the final mesh has been generated, it is saved as: a shapefile for use in a GIS, an unstructured mesh file (vtu) for visualization in ParaView, and a JSON-based text format for use in a model.

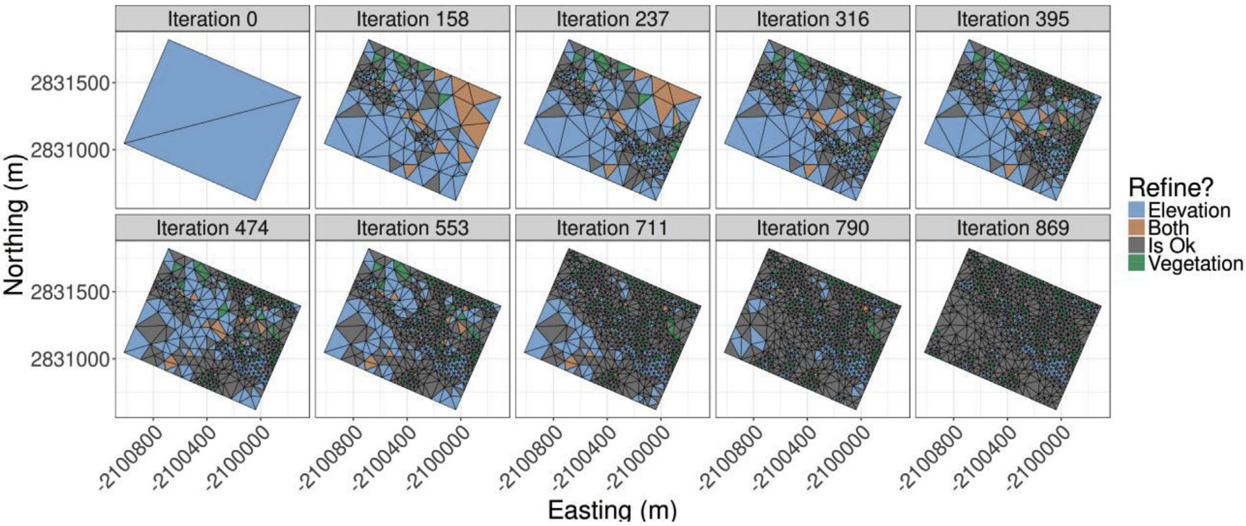

Fig. 4. Output from the meshing algorithm at various stages of refinement for a vegetated hillslope (detailed in Section 3; shown in Fig. 8). The triangulation is optimizing for elevation and vegetation cover. Initially two PLSG filling triangles are inserted into the domain. Due to the high RMSE with elevation, these are rejected, and small triangles are inserted into the domain. As the meshing continues, increasingly small triangles are inserted along the ridge-valley interface (middle of domain). The upper plateau (left hand side) is relatively flat with homogenous vegetation and therefore converges early. At the end, the triangles on the right-hand side plateau (location of patchy vegetation) require further refinement. However, these triangles have been refined to the minimum triangle size – they are therefore unconditionally accepted.

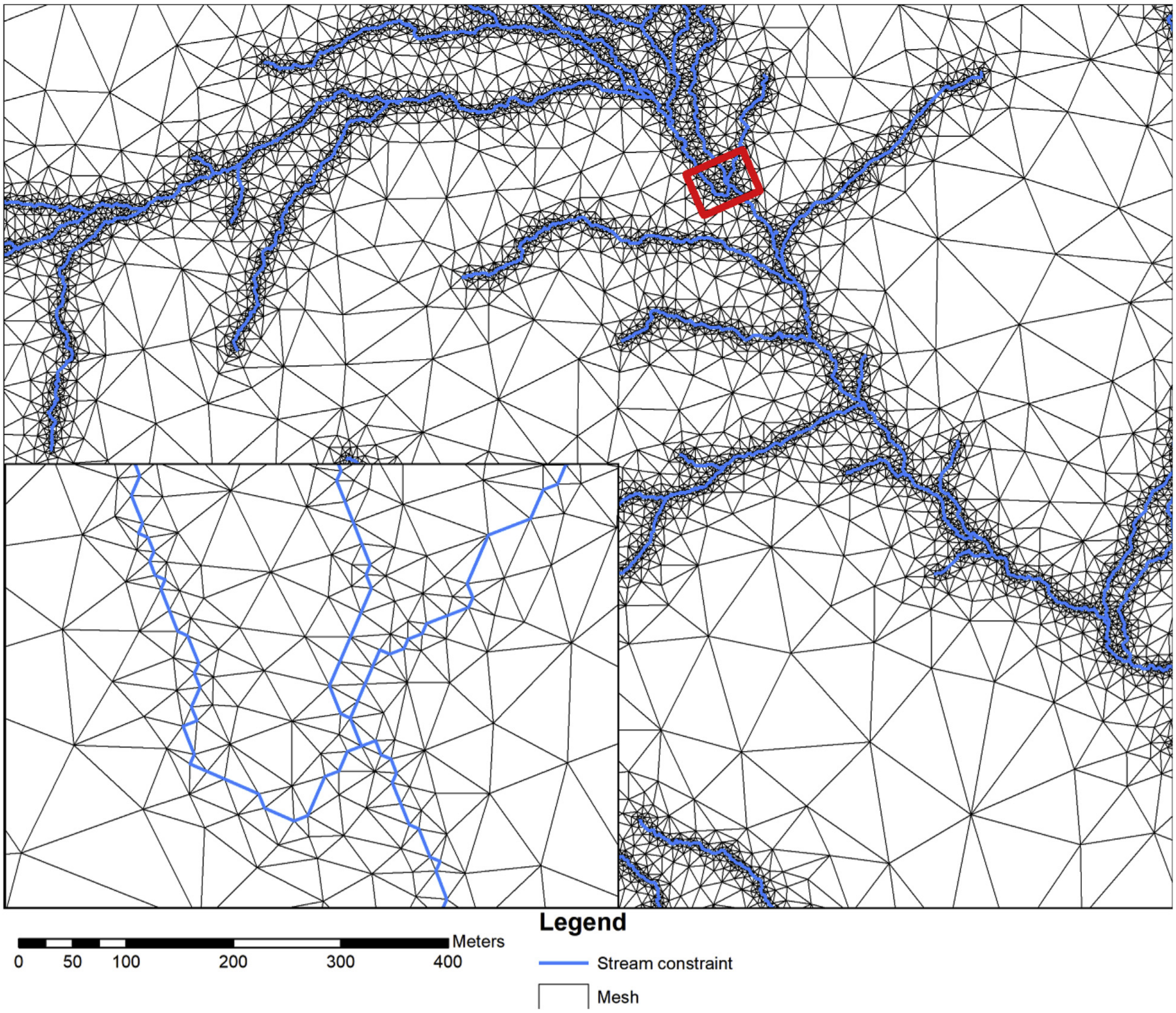

Fig. 5. A flat plane corresponding to the Granger creek sub-basin (section 3; Fig. 8) was constrained with an *a priori* stream network. A small inset shows the constraint in blue along with the mesh in black. (For interpretation of the references to colour in this figure legend, the reader is referred to the Web version of this article.)

2.3. Hydrology considerations

Shape files that describe important features, e.g. rivers and roads, can be used to constrain the triangulation. An example is shown in Fig. 5 where a flat plane has been constrained to an *a priori* determined stream network. Fig. 6 demonstrates using flow accumulation (D8 (O'Callaghan and Marks, 1984)), calculated using the RichDEM (Barnes, 2017) tool, to constrain input. Triangles are coloured using the $\log_{10}$ of the flow accumulation where high flow accumulations such as streams occur, and low flow accumulations are shown in blue. The main stream network is visible. Smaller triangles are present along these flow paths with a gradation towards larger triangles on the uplands.

3. Methodology

3.1. Spatial domain

3.1.1. Wolf Creek

The 179 km^2 Wolf Creek Research Basin, located in the Coast Mountains near Whitehorse, Yukon Territory, Canada, was used to test the meshing algorithm. It consists of three main vegetation covers: boreal forest, shrub-tundra, and sparse tundra (Pomeroy et al., 2006). Elevation ranges from 654 m to 2080 m. A 1 m × 1 m resolution LiDAR derived DEM is available for this basin, with 3.6×10^8 data cells. This is shown in Fig. 7. Vegetation classes (17 in total) are available via the Landsat-7 derived Earth Observation for Sustainable Development of Forests (EOSD) (Wulder and Nelson, 2003; Wulder et al., 2007) 25 m × 25 m vegetation classification, shown in Table 1.

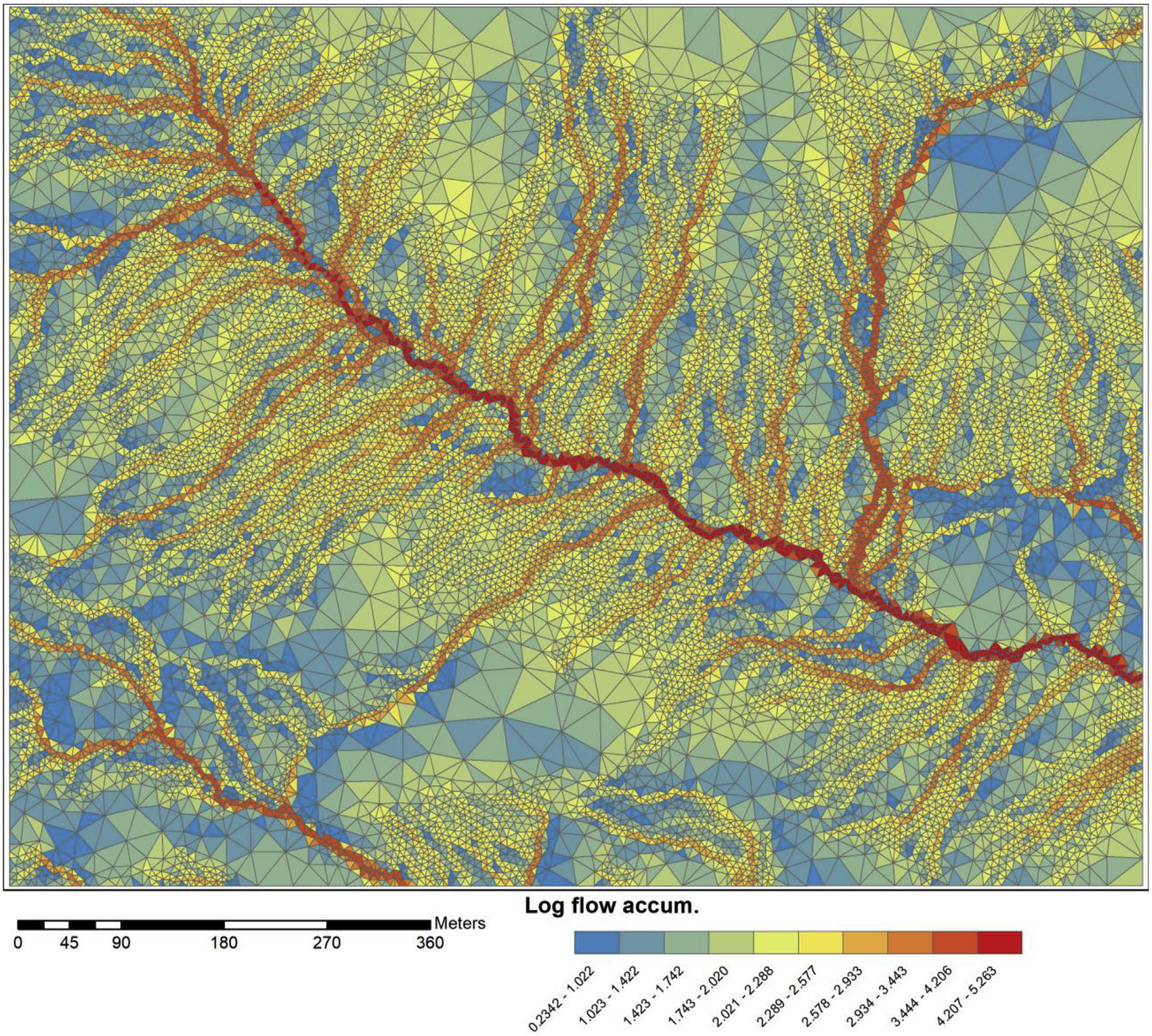

Fig. 6. A flow accumulation raster was used to conform the triangulation, in addition to elevation. Shown is the $\log_{10}$ of the calculated flow accumulation where high flow accumulation (e.g., stream) is shown in red, and low flow accumulation (e.g., source area) is shown in blue. Small triangles are present along the high flow paths, and larger triangles in the low flow accumulation areas on the uplands. (For interpretation of the references to colour in this figure legend, the reader is referred to the Web version of this article.)

3.1.2. Granger Creek

A tributary stream feeding Wolf Creek is the 8 km^2 Granger Creek sub-basin (McCartney et al., 2006). A sub-area of Granger Creek, shown as a black and white extent in Fig. 7 and expanded in Fig. 8. This domain is 1089 m × 867 m (1 m × 1 m resolution; LiDAR derived; #cells = 944,163). Topographically, this area has two upper plateaux divided by moderately steep slopes (approx. 50°) and a lower valley bottom filled with tall shrubs (McCartney et al., 2006; Dornes et al., 2008b).

3.2. Mesh quality comparison

Three meshes were generated for the sub-area of Granger Creek sub-basin: one by ArcGIS tools and two by Mesher. The ArcGIS TIN is constrained to tolerance = 1 m, and the Mesher algorithm mesh is constrained to tolerance = 1 m and to an RMSE = 1 m.

To diagnose mesh generation for a larger extent, all of the Wolf Creek Research Basin was used. Various combinations of tolerance and minimum triangle area were used to determine the impact on generated meshes. These tests used a single-objective constraint to the topography. RMSE values were: 1 m, 2 m, 5 m, 10 m, 25 m, 50 m, and 100 m. Minimum triangle areas were: 2 m^2, 4 m^2, 100 m^2, 900 m^2, 10,000 m^2, 90,000 m^2, and 100,000 m^2.

3.3. Spatial heterogeneity

Because vegetation is a patchy and spatially heterogeneous component of the surface, it provides a useful test-case for the capability of the multi-objective constraint. The use of vegetation is only meant to illustrate and test the meshing algorithm; in principle, any other surface

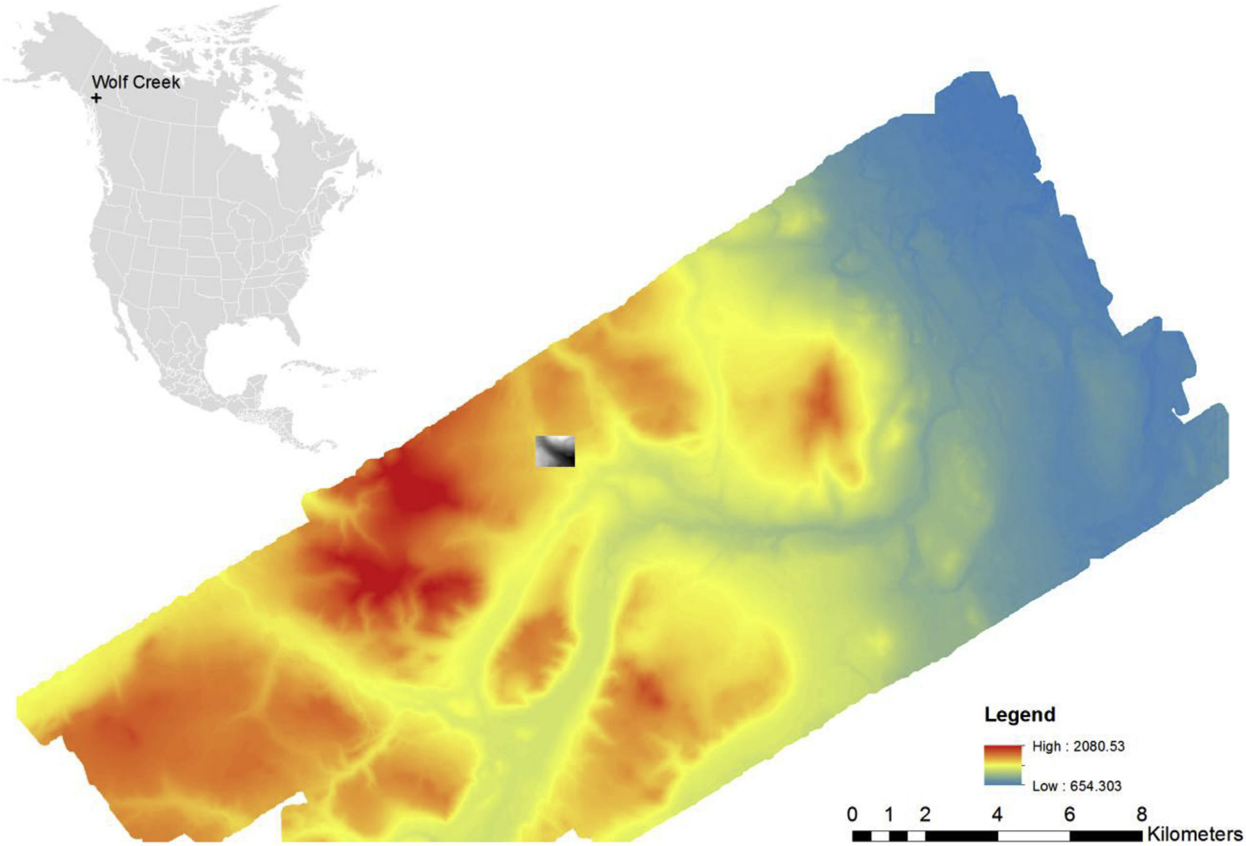

Fig. 7. Wolf Creek Research Basin LiDAR derived 1 m^2 DEM. The sub-area of the Granger-Creek sub-basin location is shown in black and white.

Table 1
Vegetation classes as derived from EOSD (25 m × 25 m) data for the Wolf Creek Research Basin.

Class number	Type	% Area
212	Coniferous-open	12
33	Exposed/Barren land	3.0
213	Coniferous-sparse	6.7
52	Shrub low (< 2 m)	50
51	Shrub tall	5.5
100	Herb (vascular, non-woody)	16
211	Coniferous-dense	2.6
221	Broadleaf-Dense	0.30
232	Mixedwood-open	0.050
32	Rock/rubble	1.5
31	Snow/ice	0.030
83	Wetland-herb	0.13
222	Broadleaf-open	0.90
20	Water	1.1
82	Wetland-shrub	0.17
81	Wetland-tree	0.030
12	Shadow	0.060

or subsurface feature can be used.

Three approximating meshes were generated: one that did not constrain to the vegetation and two that did. The two constrained meshes required > 50% and > 75% of a triangle to be covered by a single vegetation class. Minimum triangle size was set to 625 m^2 (25 m × 25 m equivalent) and RMSE = 1 m for all meshes.

To identify disjoint patches of vegetation, a connected components labelling algorithm was used (Chang and Chen, 2003). The fractal dimension was calculated for each of these patches that quantifies the complexity of planar shapes using perimeter-area scaling relationships (McGarigal and Marks, 1994). Values vary between 1 (simple Euclidean shapes) and 2 (more complex, non-Euclidean). For instance, snow patches on the ground (Shook et al., 1993a; 1993b) and in forest canopies (Pomeroy and Schmidt, 1993) around the world have $D \approx 1.3$. For a patch with perimeter P and area A, the fractal dimension D relates the two as

$$P = kA^{D/2}, \tag{5}$$

where k is a scale coefficient related to the resolution of measurement. To calculate the fractal dimensions of the meshes, the three triangular meshes were rasterized to a 25 m × 25 m raster, corresponding to the original EOSD data set. Both the connected components labelling algorithm and the fractal dimension calculation were computed via the R package SDMTools (VanDerWal, 2016).

The distribution of fractal dimensions and thus the patch complexity between the original and unstructured mesh should be similar. Quantile-quantile (Q-Q) plots allow for visually diagnosing differences between distributions. The two-sample Kolmogorov-Smirnov (K-S) (Conover, 1971) test was used to statistically compare the distributions. This is a non-parametric test that determines if two probability distributions originate in the same distribution. The null hypothesis is that the two test distributions originate in the same distribution. Significance was determined for $p < 0.01$.

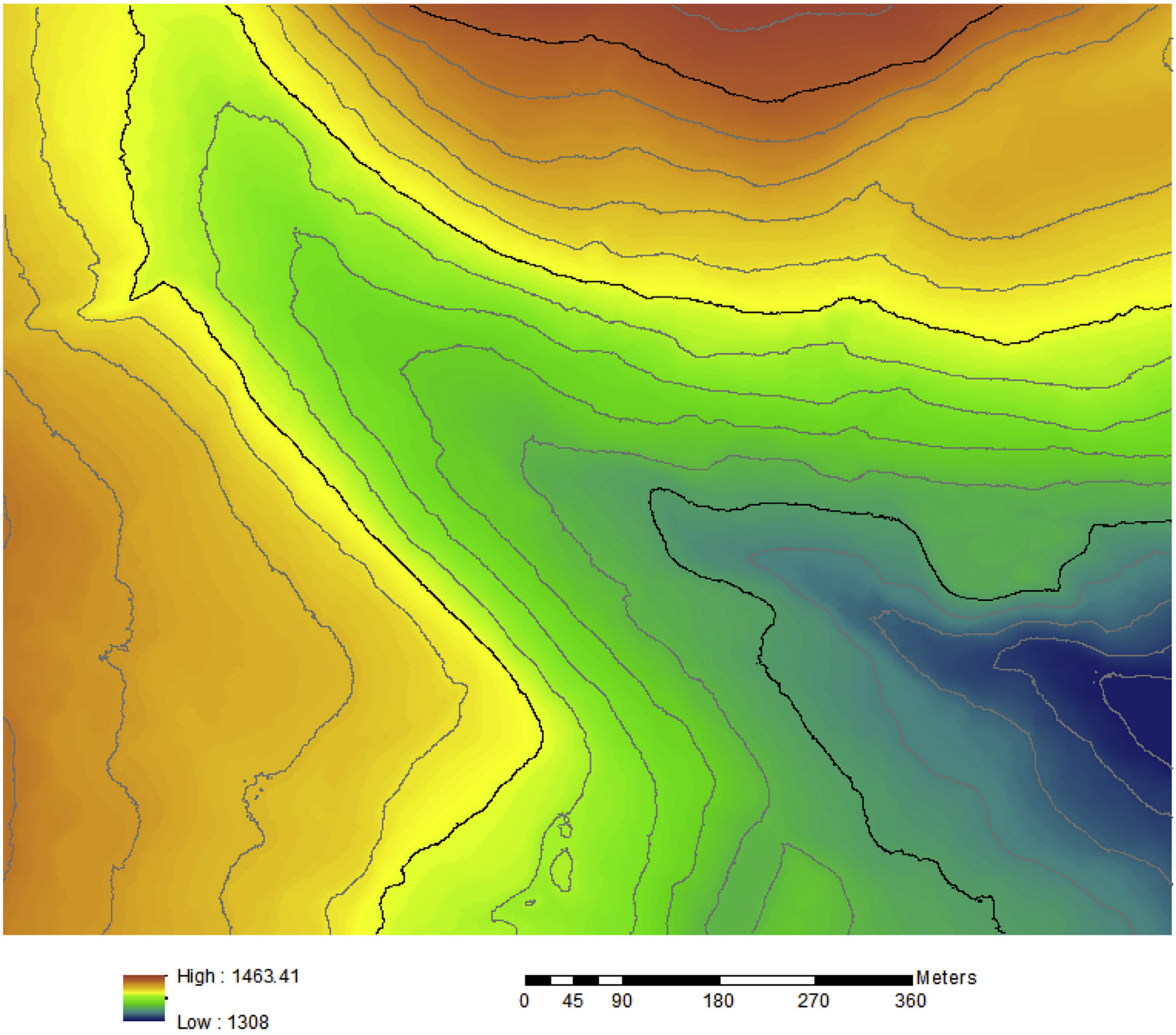

Fig. 8. Small valley sub-area of the Granger Creek valley. LiDAR DEM at 1 m × 1 m resolution. Contours are every 10 m (grey) and 50 m (black). The domain is approximately 1000 m by 900 m.

In addition to the patch geometry, patch area should also be preserved. This is visually tested via Korcak's law, an empirical size-distribution for geographical objects (Imre and Novotný, 2016). These results are shown via Korcak plots where the (normalized) number of areas that are in exceedance excess $F(a)$ of a threshold area A are plotted versus the area. The patch area distributions were statistically compared using the K-S test. Significance was determined for $p < 0.01$.

In summary, the per-patch complexity metric distribution and per-patch area distribution for three unstructured meshes, each with an increasingly strict vegetation criterion, were compared against the distributions derived from the original vegetation raster dataset. If the distributions are significantly different, then it can be surmised that the unstructured mesh is not correctly capturing the heterogeneity.

3.4. *Weighting*

The sub-basin domain was meshed using the weighting algorithm for two test cases. In all cases, the elevation tolerance was given as 5 m, with a minimum triangle area of 5 m × 5 m. For the high weight case, vegetation was given a weight of 0.8. For the low weight case, vegetation was given a weight of 0.2. A cut-off weight threshold of 0.8 was used.

3.5. *Performance tests*

Performance tests were done on a workstation with an Intel Dual Intel Xeon E5-2630 (six core HT, 2.6 GHz) CPU, 128 GB DDR3 ECC RAM, and 7200 rpm mechanical harddrive, running Ubuntu 14.10. The

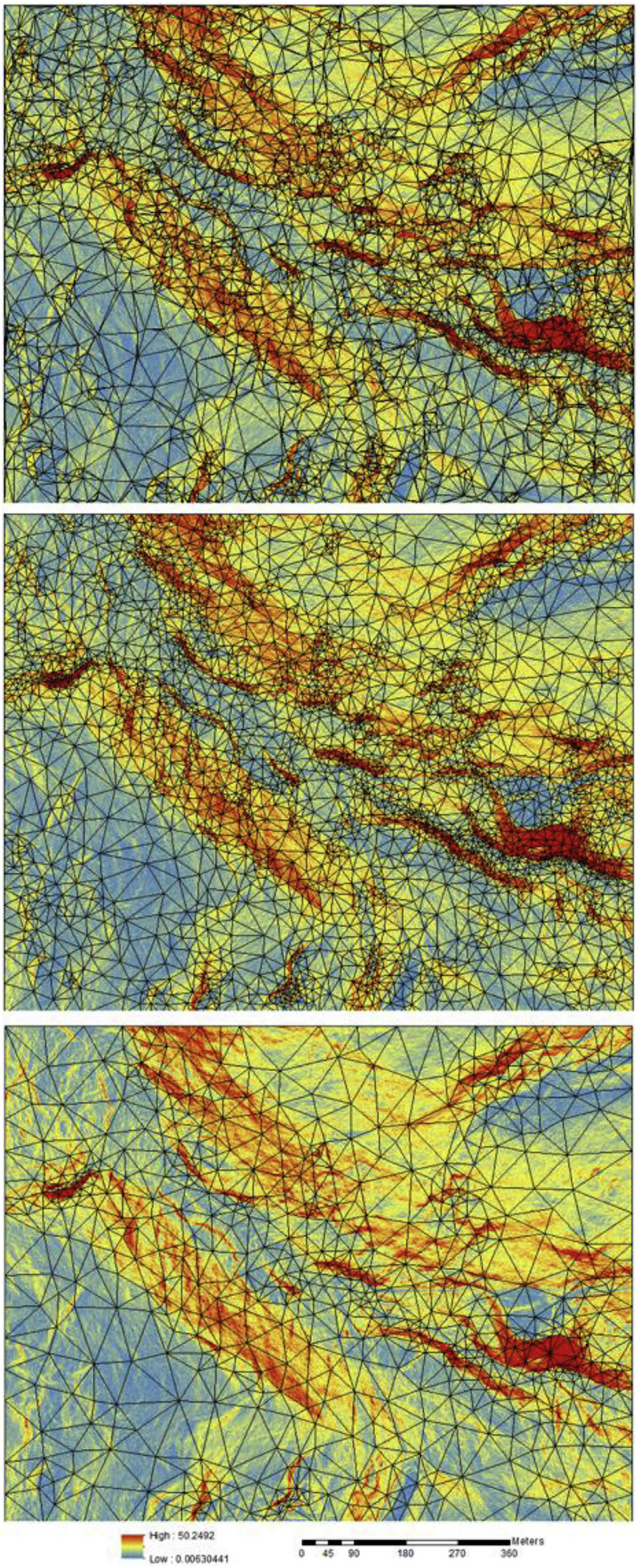

Fig. 9. Triangulations generated from a LiDAR DEM (1 m × 1 m resolution) for the Granger Creek sub-area. Colours represent slope where red = 50° and blue = 0°. Top) ArcGIS TIN generation tools using a 1 m tolerance. Number of triangles = 8346. Middle) Mesher mesh using a 1 m tolerance. Number of triangles = 6107. Bottom) Mesher mesh using a 1 m RMSE threshold. Number of triangles = 1424. (For interpretation of the references to colour in this figure legend, the reader is referred to the Web version of this article.)

domain used was the Wolf Creek domain. Tolerances used were 1 m, 2 m, 5 m, 10 m, 25 m, 50 m, and 100 m. Minimum triangle areas were 2 m^2, 4 m^2, 100 m^2, 900 m^2, 10,000 m^2, 90,000 m^2, and 100,000 m^2. Each tolerance-area combination was run five times, taking the minimum wall-clock time. Wall-clock times include the entirety of the pre- and post-processing steps. Therefore, some disk I/O performance is implicitly measured.

4. Results

4.1. Mesh quality comparison

An unstructured mesh generated with ArcGIS (tolerance = 1 m) is shown in Fig. 9 (top). Behind the mesh (black lines), the slope is shown in colour, with high slope in red (50°) and low slope in blue (0°). The mesh generation has produced fewer, larger triangles on the upper plateaus and more, smaller triangles along the hill slopes. This mesh demonstrates the generation of poorly shaped (i.e., long and skinny) triangles due to no constraint on minimum inner angles. There are 8346 triangles in this domain, compared to 944,163 raster cells (0.88% of the raster cells).

The unstructured mesh generated with Mesher (tolerance = 1 m) is shown in Fig. 9 (middle). Like the ArcGIS output, the plateaus have larger triangles and the steep slopes have smaller triangles. Due to the inner-angle constraint, there are no long skinny triangles, and there is a smooth gradation between large and small triangles. This is especially evident along the steep slopes. Fewer triangles were generated than ArcGIS; 6107 (0.65% of the raster cells). The mesh generated with a 1 m RMSE threshold using Mesher is shown in Fig. 9 (bottom). There are 1424 triangles in this domain (0.15% of raster cells). Fewer small triangles have been generated for the high slope areas versus the tolerance methods.

The distributions (normalized density) of the attributes of each mesh are shown in Fig. 10, with the top showing the RMSE (m), the middle showing the internal triangle angles (degrees), and the bottom showing triangle area (m^2). For both tolerance methods, Mesher and ArcGIS produce almost identical RMSE distributions. Although both the ArcGIS and Mesher meshes were constrained to a 1 m maximum tolerance, an over-representation of the terrain has occurred, as shown by the low RMSE values. The tolerance of 1 m resulted in a maximum RMSE of approximately 0.5 m–0.6 m. The ArcGIS mesh has many small-angled, skinny triangles, making for sharp transitions between areas. This is undesirable for numerical usage and leads to a 36% increase in total number of triangles versus Mesher's tolerance mesh. The 1 m RMSE mesh resulted in an almost identical distribution of inner angles as that of the Mesher tolerance mesh and a more uniform RMSE distribution is found.

4.2. Tolerance – minimum area relationship

The number of triangles produced for various combinations of error (RMSE) and minimum triangle areas (m^2) for the entire Wolf Creek domain are shown in Fig. 11 (note log axes). The *x*-axis shows the minimum triangle area. Various approximations to the elevation (RMSE [m]) are shown in coloured lines. Vegetation constraints are shown in the facets for 0%, 50% (0.5), and 75% (0.75) area constraint. The highest-accuracy mesh is the 1 m RMSE mesh and shows a rapid reduction in total elements as the minimum area increases. As the tolerances increase, there is a move towards a log-linear relationship between the number of triangles and minimum area. Because a triangle's minimum area overrides the tolerance calculation, the large area and high RMSEs combinations produce few triangles regardless of the tolerances provided. The finest mesh with 1 m RMSE and 2 m^2 minimum triangle area has approximately 454,000 triangles. This corresponds to a reduction of 50% in total number of elements versus the raster. A large spread in total number of triangles is found in the 0% vegetation

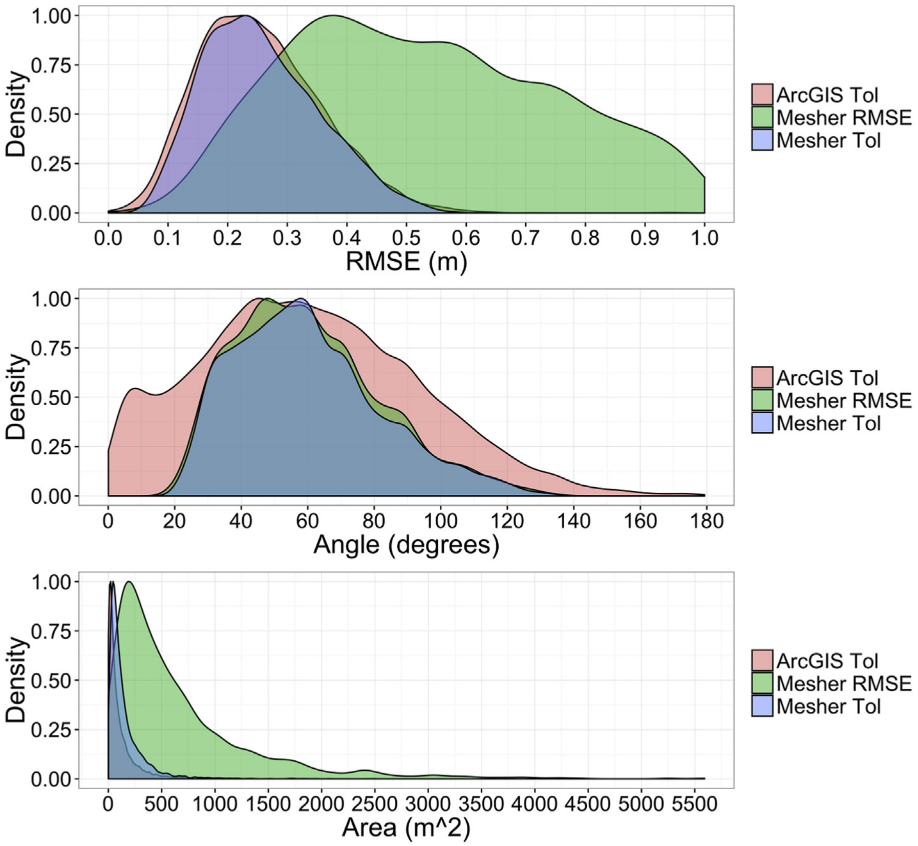

Fig. 10. Root Mean Square Error (RMSE (m)), inner triangle area (degrees), and triangle area (m^2) for the meshes shown in Fig. 9.

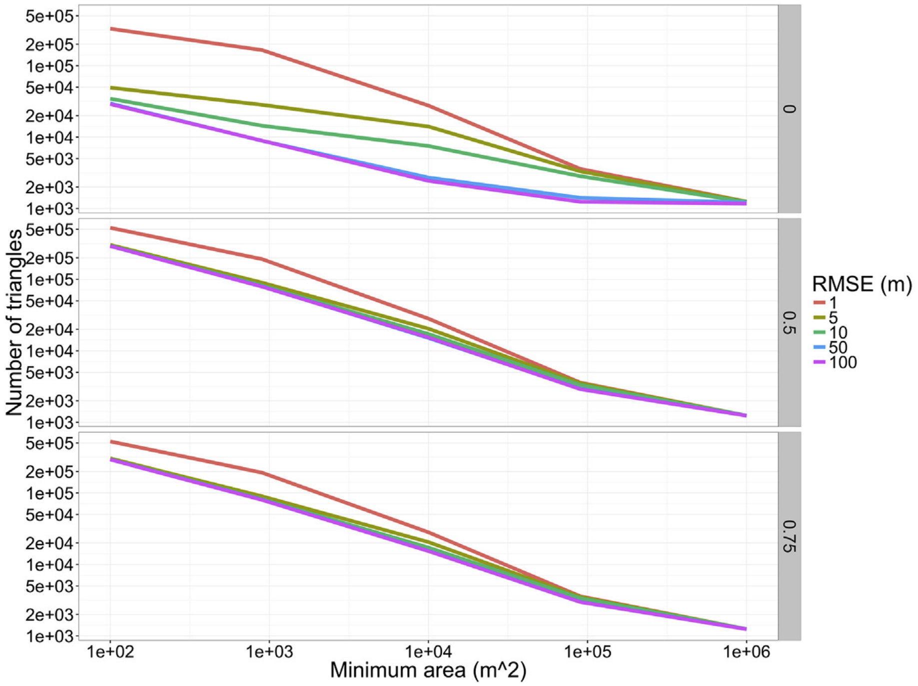

Fig. 11. Number of triangles as a function of minimum triangle area (*x*-axis) and RMSE tolerance. Note log axes. The facets corresponds to a vegetation fraction constraint of 0 (top), 0.5 (middle), and 0.75 (bottom).

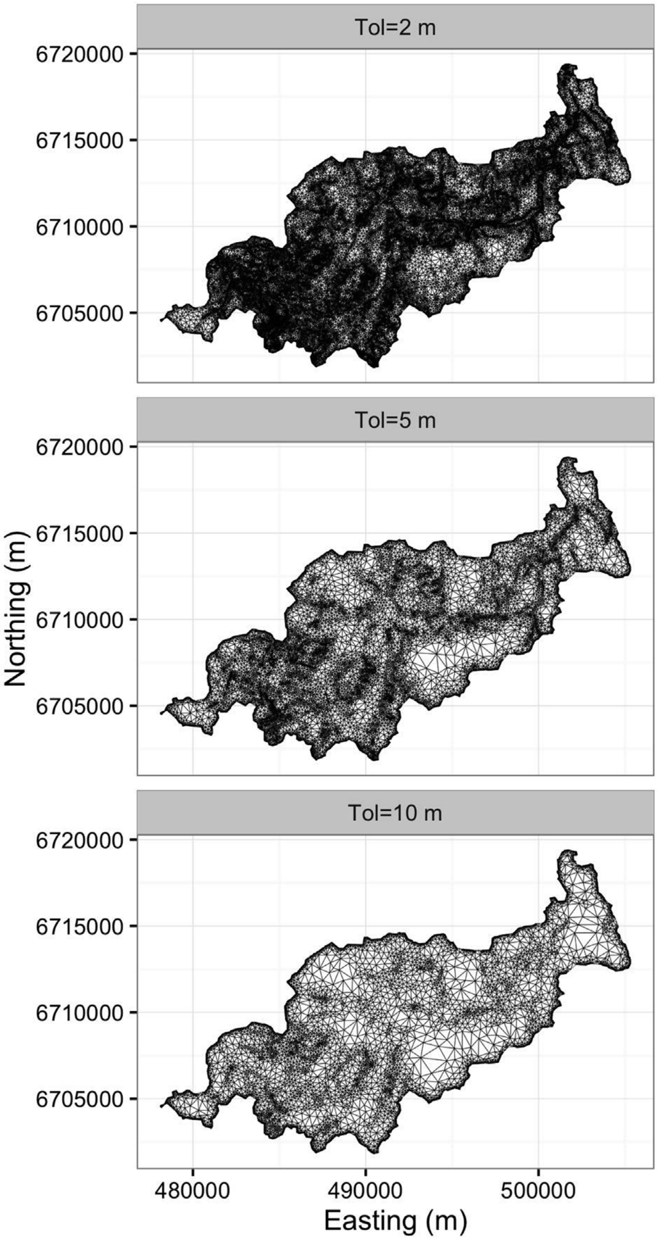

Fig. 12. Comparison of three meshes showing impact of tolerance: 2 m (top), 5 m (middle), 10 m (bottom) and a minimum area of 90,000 m^2 (300 m × 300 m raster equivalent).

case between all RMSE values. However, as the 50% and 75% constraints are added, all but the 1 m RMSE have almost identical numbers of total triangles produced.

Shown in Fig. 12 are three mesh outputs for RMSE tolerances 2 m, 5 m, and 10 m in combination with a maximum triangle area of 90,000 m^2 (300 m × 300 m raster equivalent). In all cases, a higher density of triangles is produced along the basin boundary. This is due to the triangulation algorithm exactly representing this boundary. In practice, this is easily mitigated by simplifying the basin boundaries. The lower tolerances (5 m and 10 m) produce fewer triangles on the upper slopes (e.g., southern portion of basin). In all cases, the more complex ridges are generally represented.

4.3. Multi-objective constraints

A mesh for the valley location in Wolf Creek is shown in Fig. 13 and was constrained to topography (RMSE = 1 m, maximum triangle area = 225 m^2 [25 m × 25 m]) and vegetation (primary vegetation class > 50%). The vegetation is shown by the 25 m × 25 m raster, with coloured cells corresponding to different vegetation (hollow cells are low shrub). It is evident that the larger vegetation locations on the north plateau (top of domain) have had a few smaller triangles inserted to capture the bounds even though larger triangles could have been used due to small topographic variability. Individual cells in the southern-western portion (bottom left) are missed owing to the 50% constraint – increasing this allows for capturing these individual raster cells at the cost of more triangles. In the east herb area (light blue), large triangles fill the middle of this landcover but are sized to capture the bounds of the patch.

Shown in Fig. 14 are the Q-Q plots of the fractal dimensions for each of the 17 vegetation classifications, across the entirety of Wolf Creek. The fractal dimensions are shown for three cases versus the original dataset: an unstructured mesh constrained to vegetation and topography for 50% constraint (red) and 75% constraint (green) and an unstructured mesh constrained to only topography (blue). Between the 50% and 75% constrained meshes, the largest impacts are in the tails of the distribution. The mesh constrained to only topography shows a substantial simplification of the vegetation patches. Table 2 shows the results from comparing the distributions of fractal dimensions of each unstructured mesh approximation to the original raster dataset via the K-S test. Table entries of $p < 0.01$ show distributions that were significantly different. Non-significant p values are not shown. This table shows that 11of 17 land classes did not accurately have their heterogeneity preserved for the topography-only mesh. There is a significant improvement in preserving heterogeneity when using the 75% versus 50% meshes. In all cases, land classes 51 and 213 appear to be the most difficult to represent. Land class 51 is short shrub and represents the largest vegetation area. In many cases, it is the 'background' vegetation class in which other patches are found. Therefore, all the small errors in the approximating mesh are likely compounded for this vegetation class, leading to the observed simplification (i.e., lower fractal dimension). Land class 213, coniferous-sparse, is highly patchy with many small discontinuous locations, likely resulting in these patches being missed. For both the 50% and 75% constraints, the small patches are well represented (e.g., class 222) versus the topography-only constraint. The unstructured mesh constrained to just topography produced 95,154 triangles, the 50% vegetation constraint produced 276,026 triangles, and the 75% vegetation constraint produced 300,308 triangles. Therefore, the increased vegetation constraint between 50% and 75% does not come at a substantial increase of triangles. However, adding the vegetation constraint roughly triples the total number of triangles versus the topography-only constraint.

The Korcak fractional exceedance of patch areas $F(a)$ versus vegetation patch areas are shown in Fig. 15for each land cover type for each of the unstructured mesh constraints: 50%, 75%, and no constraint. By visual inspection, each of the tighter constraints produces an $F(a)$-area relationship that more closely matches the baseline dataset. Numerically, this is validated in Table 3. Table entries of $p < 0.01$ show distributions that were significantly different. Non-significant p values are not shown. This table shows that 11 of 17 vegetation classes did not accurately have their heterogeneity preserved for the topography-only mesh. In all cases, this analysis supports the results shown in Table 2.

4.4. Weighted constraints

A comparison between weighted constraints for vegetation are

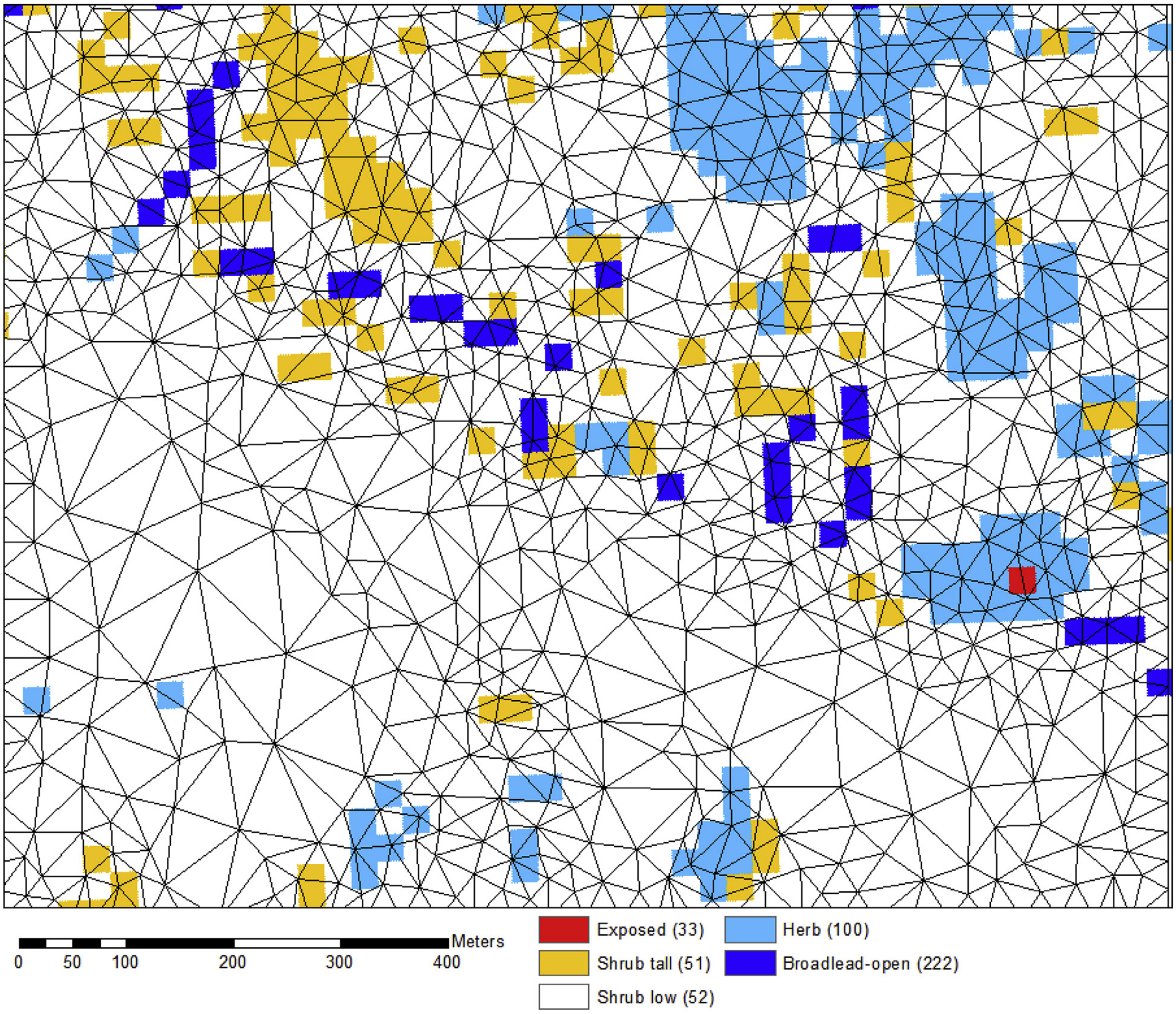

Fig. 13. Sub-area of the Grange Creek sub-basin, constrained to topography (RMSE = 1 m, maximum triangle area = 225 m^2 [25 m × 25 m]) and to vegetation (dominant class > 50%). Vegetation from the EOSD raster is shown in colour. (For interpretation of the references to colour in this figure legend, the reader is referred to the Web version of this article.)

shown in Fig. 16. Due to the coarse topographic tolerance and the low vegetation weight, ensures that the meshing algorithm almost entirely ignores the vegetation. This is compared to the high vegetation weight, where, despite fulfilling the coarse elevation tolerance, triangles are refined further to capture the vegetation patches.

4.5. Wall-clock performance

Wall-clock times(s) to generate the mesh for the Wolf Creek basin are shown in Fig. 17 for each combination of RMSE values delineated by marker symbol, minimum areas delineated by colour) and three vegetation constraints delineated by line type. These wall-clock times are shown as a function of total number of triangles in the final mesh. The increase in wall-clock time is approximately linear. The inclusion of the vegetation constraint did not require substantially more wall-clock time. The wall-clock time for generating the finest mesh with RMSE = 1 m was minimally different than the 50% and 75% vegetation constraint wall-clock times. The average wall-clock time of the two vegetation constraints shows that for the worst case there is a 40% increase in computational time. This increase only appears to be present in the highest resolution meshes. As the minimum area decreases, the algorithm is less able to avoid calls to the tolerance calculation as well as the secondary constraints.

5. Conclusion

The use of a variable-resolution unstructured mesh allows for fine resolution in areas of high spatial variability and coarse resolution in areas of low spatial variability. Many of the existing triangulation methods either sacrifice triangle quality (e.g., VIP, Heuristic, skeleton) to introduce this resolution variability or guarantees well-formed uniform meshes (e.g., constrained Delaunay triangulation) at the expense

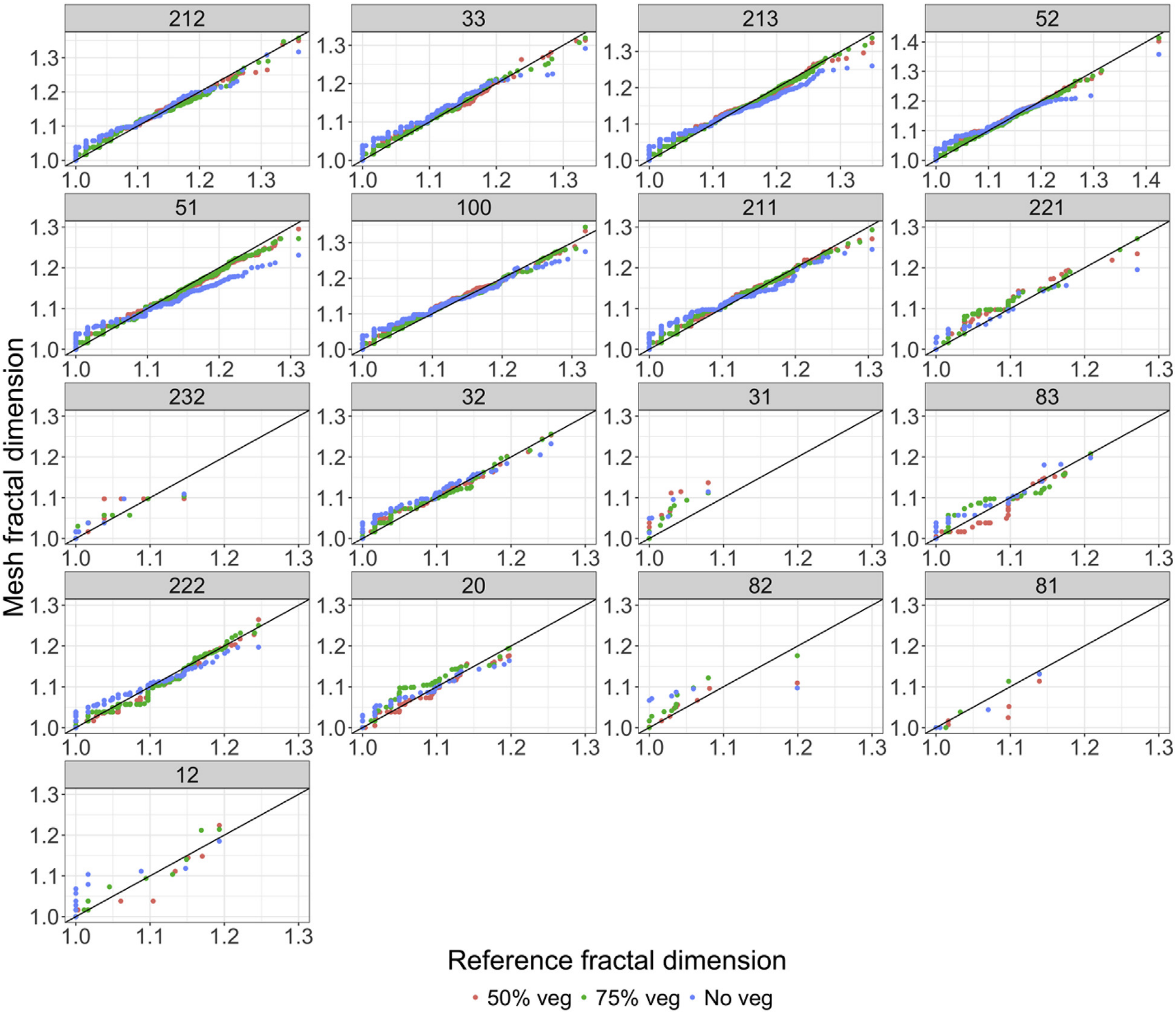

Fig. 14. Q-Q plots of fractal dimensions for each landcover for both unstructured mesh approximations (constrained to vegetation (50%), red; constrained to vegetation (75%), green; only topographic constraint, blue), versus the original raster dataset. (For interpretation of the references to colour in this figure legend, the reader is referred to the Web version of this article.)

of variable triangle resolution.

This work introduced a triangle selection method that coupled per-triangle error metrics, such as RMSE, with a constrained Delaunay triangulation. It was shown that such a method produces well-graded, well-formed triangles that allow for a variable spatial resolution. Using an RMSE error metric provides a better distribution of triangle sizes and errors compared to the maximum difference metric used in existing tools. Compared to the widely used mesh generation in ArcGIS, the Mesher software produced higher-quality triangles, as diagnosed by the distribution of triangle shape and size, and did not lead to an over-representation of the terrain due to its more robust error metric. A single-objective method was extended to allow for constraining to an arbitrary set of rasters. This multi-objective approach allowed for using other hydrologically important data, such as vegetation and soil data, to ensure the spatial heterogeneity of these data is preserved, even when the topography is homogenous and warrants few triangles. The fractal dimension of vegetation patch perimeter-area relationships was used as a measure of spatial heterogeneity in a secondary hydrological variable. By considering a secondary objective raster, the spatial heterogeneity was better preserved than by only constraining to the topography. Compared to a LiDAR raster, 50%–99.9% of the total number of elements can be removed while preserving the spatial heterogeneity of topography as well as secondary landscape features due to the multi-objective refinement approach.

Source code

The Mesher software is open source under the GPLv3 license and is available at github. com/Chrismarsh/mesher.

Author contribution

C. Marsh: Initial idea, coding, analysis, manuscript preparation.

R. Spiteri: Idea refinement, manuscript revision.

J. Pomeroy: Idea refinement, analysis refinement, manuscript revision.

H. Wheater: Idea refinement, manuscript revision.

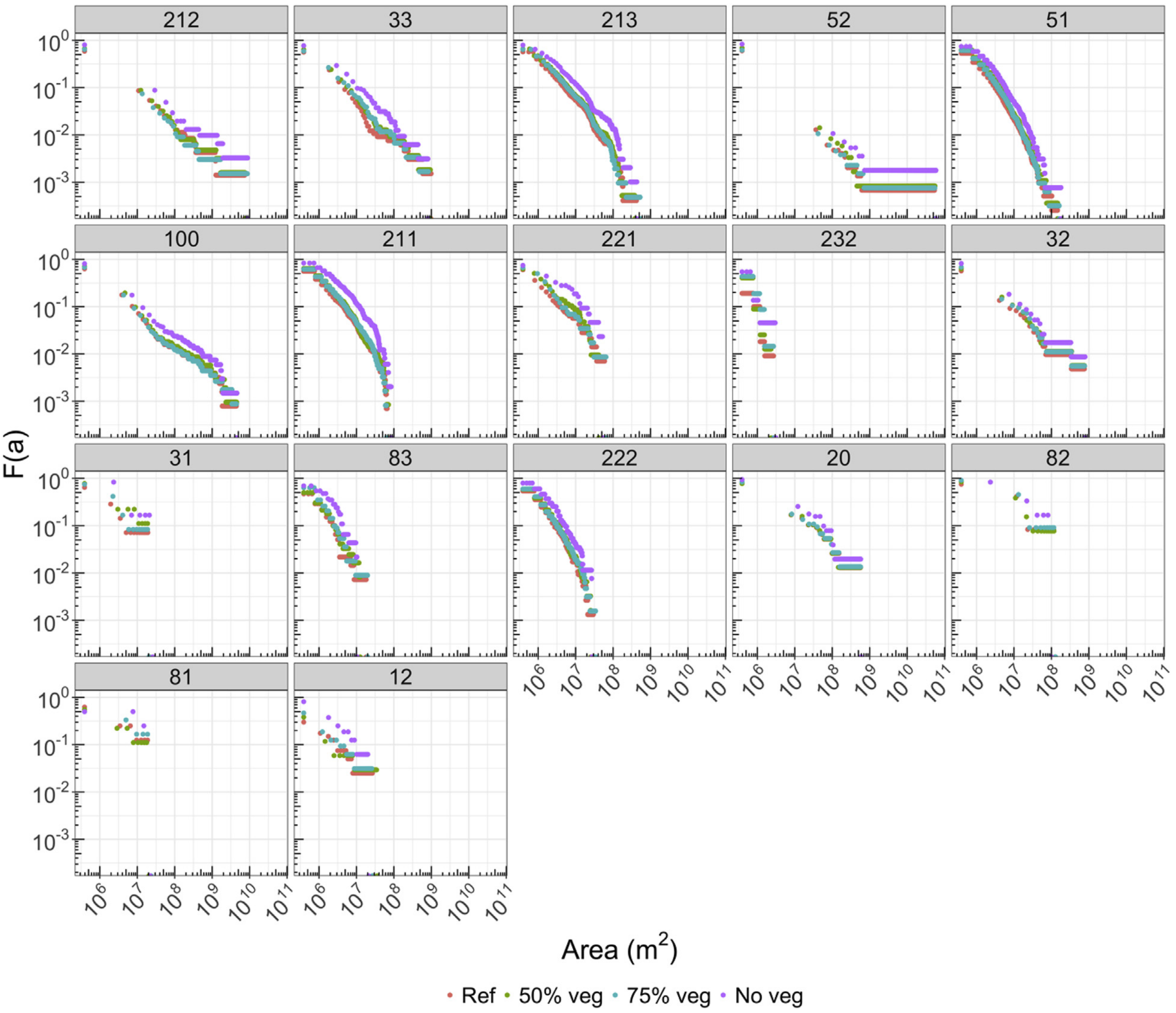

Fig. 15. Korcak fractional exceedance area *F(a)* versus area for each landcover for both unstructured mesh approximations (constrained to vegetation (50%), green; constrained to vegetation (75%), blue; only topographic constraint, purple), versus the original raster dataset (red). (For interpretation of the references to colour in this figure legend, the reader is referred to the Web version of this article.)

Table 2
Kolmogorov-Smirnov tests of fractal index distributions for: non-vegetation constraint, 50%, and 75% vegetation area constraint versus original vegetation raster. Significance was determined for $p < 0.01$ and denotes the distributions are significantly different. Only significantly different distributions are listed. Distribution differences implies the approximating mesh did not capture the heterogeneity and patch complexity of the vegetation patches.

Class number	Type	Veg constraint 50	Veg constraint 75	No veg constraint
212	Coniferous-open			$p < 0.01$
33	Exposed/Barren land			$p < 0.01$
213	Coniferous-sparse	$p < 0.01$	$p < 0.01$	$p < 0.01$
52	Shrub low (< 2 m)	$p < 0.01$		$p < 0.01$
51	Shrub tall	$p < 0.01$	$p < 0.01$	$p < 0.01$
100	Herb (vascular, non-woody)	$p < 0.01$		$p < 0.01$
211	Coniferous-dense	$p < 0.01$		$p < 0.01$
221	Broadleaf-Dense			
232	Mixedwood-open			
32	Rock/rubble			$p < 0.01$
31	Snow/ice			
83	Wetland-herb			
222	Broadleaf-open			$p < 0.01$
20	Water			
82	Wetland-shrub			$p < 0.01$
81	Wetland-tree			
12	Shadow			$p < 0.01$

Table 3

Kolmogorov-Smirnov tests of patch area distributions for: non-vegetation constraint, 50%, and 75% vegetation area constraint versus original vegetation raster. Significance was determined for $p < 0.01$, and denotes the distributions are significantly different. Only significantly different distributions are listed. Distribution differences imply the approximating mesh did not capture the area of the vegetation patches.

Class number	Type	Veg constraint 50	Veg constraint 75	No veg constraint
212	Coniferous-open			$p < 0.01$
33	Exposed/Barren land			$p < 0.01$
213	Coniferous-sparse	$p < 0.01$	$p < 0.01$	$p < 0.01$
52	Shrub low (< 2 m)	$p < 0.01$		$p < 0.01$
51	Shrub tall	$p < 0.01$	$p < 0.01$	$p < 0.01$
100	Herb (vascular, non-woody)	$p < 0.01$		$p < 0.01$
211	Coniferous-dense	$p < 0.01$		$p < 0.01$
221	Broadleaf-Dense			
232	Mixedwood-open			
32	Rock/rubble			$p < 0.01$
31	Snow/ice			
83	Wetland-herb			
222	Broadleaf-open			$p < 0.01$
20	Water			
82	Wetland-shrub			$p < 0.01$
81	Wetland-tree			
12	Shadow			$p < 0.01$

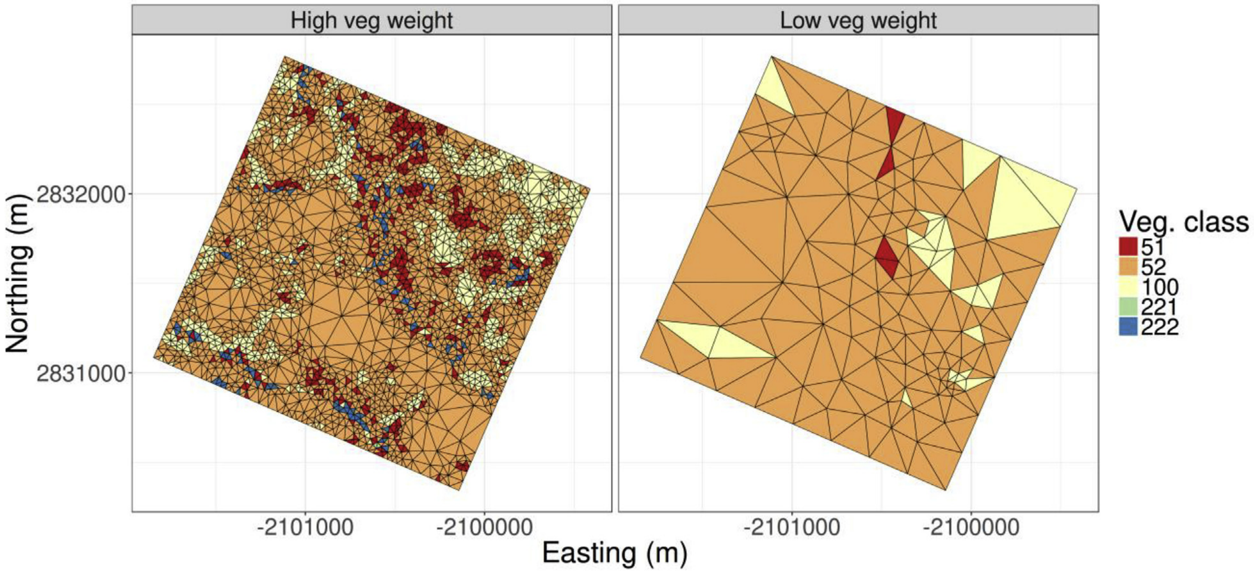

Fig. 16. Comparison of high vegetation weight (left) and low vegetation weight (right). A coarse elevation tolerance was used. Therefore, for the low vegetation weight, the meshing algorithm almost entirely ignores the vegetation patches. For the high vegetation weight, despite fulfilling the elevation tolerances, the mesh is subsequently refined further to capture the vegetation boundaries.

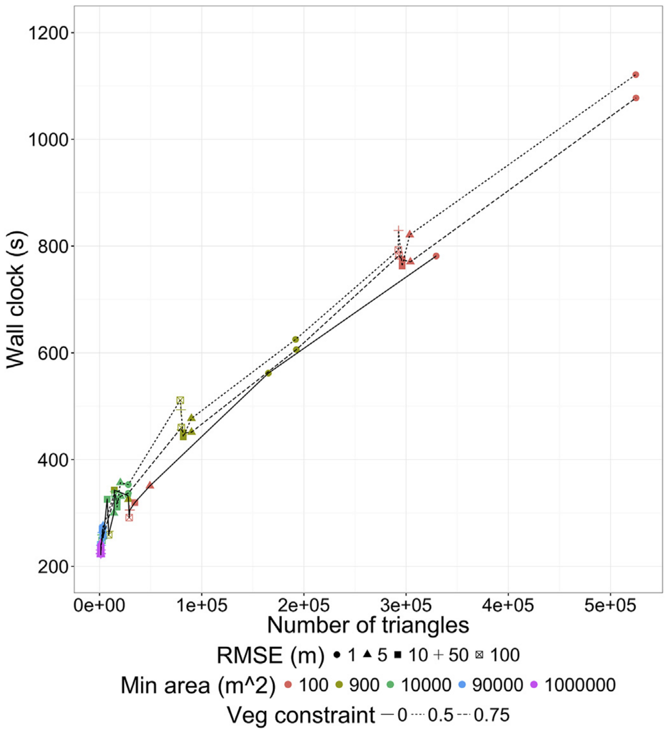

Fig. 17. Wall-clock times as a function of total number of triangles. The marker symbols demote the tolerances (RMSE threshold), the colours denote the minimum areas (m^2), and the line types show these for each vegetation constraint (fractional percent). (For interpretation of the references to colour in this figure legend, the reader is referred to the Web version of this article.)

Acknowledgments

The authors would like to thank the NSERC Changing Cold Regions Network, NSERC Discovery Grants, NSERC Alexander Graham Bell Scholarships, the Canada Excellence Research Chairs and Canada Research Chairs programmes and Yukon Environment for funding. The provision of Granger Creek data by J. Richard Janowicz of Yukon Environment is greatly appreciated. Discussion with and code testing by Nicholas Wayand is greatly appreciated. The authors would like to thank the handling editor Richard Barnes for helpful comments, in addition to the three anonymous peer reviewers whose comments improved the quality of this manuscript.

References

Barnes, R., 2017. Parallel non-divergent flow accumulation for trillion cell digital elevation models on desktops or clusters. Environ. Model. Software 92, 202–212. http://dx.doi.org/10.1016/j.envsoft.2017.02.022.

Berger, M.J., Colella, P., 1989. Local adaptive mesh refinement for shock hydrodynamics. J. Comput. Phys. 82 (1), 64–84. http://dx.doi.org/10.1016/0021-9991(89)90035-1.

Bilskie, M.V., Hagen, S.C., 2013. Topographic accuracy assessment of bare earth lidar-derived unstructured meshes. Adv. Water Resour. 52, 165–177. http://dx.doi.org/10.1016/j.advwatres.2012.09.003.

Bilskie, M.V., Coggin, D., Hagen, S.C., Medeiros, S.C., 2015. Terrain-driven unstructured mesh development through semi-automatic vertical feature extraction. Adv. Water Resour. 86, 102–118. http://dx.doi.org/10.1016/j.advwatres.2015.09.020.

Carey, S.K., Woo, M., 2001. Spatial variability of hillslope water balance, wolf creek basin, subarctic yukon. Hydrol. Process. 15 (16), 3113–3132. http://dx.doi.org/10.1002/hyp.319.

Caviedes-Voullième, D., García-Navarro, P., Murillo, J., 2012. Influence of mesh structure on 2D full shallow water equations and SCS Curve Number simulation of rainfall/runoff events. J. Hydrol. 448–449, 39–59. http://dx.doi.org/10.1016/j.jhydrol.2012.04.006.

Chang, F., Chen, C.J., 2003. A component-labeling algorithm using contour tracing technique. In: Proc. Int. Conf. Doc. Anal. Recognition, *ICDAR, 2003–Janua*, vols. 741–745http://dx.doi.org/10.1109/ICDAR.2003.1227760.

Chang, K., 2008. Introduction to Geographic Information Systems. McGraw-Hill, New York, New York, USA.

Conover, W.J., 1971. Practical Nonparametric Statistics. John Wiley & Sons, New York.

Debeer, C.M., Pomeroy, J.W., 2017. Influence of snowpack and melt energy heterogeneity on snow cover depletion and snowmelt runoff simulation in a cold mountain environment. J. Hydrol. 553, 199–213. http://dx.doi.org/10.1016/j.jhydrol.2017.07.051.

Dornes, P.F., Pomeroy, J.W., Pietroniro, A., Verseghy, D.L., 2008a. Effects of spatial aggregation of initial conditions and forcing data on modeling snowmelt using a land surface scheme. J. Hydrometeorol. 9 (4), 789–803. http://dx.doi.org/10.1175/2007JHM958.1.

Dornes, P.F., Pomeroy, J.W., Pietroniro, A., Carey, S.K., Quinton, W.L., 2008b. Influence of landscape aggregation in modelling snow-cover ablation and snowmelt runoff in a sub-arctic mountainous environment. Hydrol. Sci. J. 53 (4), 725–740.

El-Shimy, N., Valeo, C., Habib, A., 2005. Digital Terrain Modeling: Acquisition, Manipulation, and Applications. Artech House, Inc., Norwood, MA.

Essery, R., Pomeroy, J., 2004. Implications of spatial distributions of snow mass and melt rate for snow-cover depletion: theoretical considerations. Ann. Glaciol. 38 (1), 261–265. http://dx.doi.org/10.3189/172756404781815275.

Essery, R., Li, L., Pomeroy, J., 1999. A distributed model of blowing snow over complex terrain. Hydrol. Process. 13 (14–15), 2423–2438. http://dx.doi.org/10.1002/(SICI)1099-1085(199910)13:14/15<2423::AID-HYP853>3.0.CO;2-U.

Foken, T., 2008. The energy balance closure problem: an overview. Ecol. Appl. 18 (6), 1351–1367. http://dx.doi.org/10.1890/06-0922.1.

GDAL Development Team, 2016. GDAL - Geospatial Data Abstraction Library, Version 2.1.1.

Gelfan, A.N.A., Pomeroy, J.W., Kuchment, L.S., 2004. Modeling forest cover influences on snow accumulation, sublimation, and melt. J. Hydrometeorol. 5 (1997), 785–804. http://dx.doi.org/10.1175/1525-7541(2004)005<0785:MFCIOS>2.0.CO;2.

Grünewald, T., Schirmer, M., Mott, R., Lehning, M., 2010. Spatial and temporal variability of snow depth and ablation rates in a small mountain catchment. Cryosphere 4 (2), 215–225. http://dx.doi.org/10.5194/tc-4-215-2010.

Hagen, S.C., Westerink, J.J., Kolar, R.L., 2000. One-dimensional finite element grids based on a localized truncation error analysis. Int. J. Numer. Meth. Fluid. 32 (2), 241–261. http://dx.doi.org/10.1002/(SICI)1097-0363(20000130)32:2<241::AID-FLD947>3.0.CO;2-#.

Hagen, S.C., Westerink, J.J., Kolar, R.L., Horstmann, O., 2001. Two-dimensional, unstructured mesh generation for tidal models. Int. J. Numer. Meth. Fluid. 35 (6), 669–686. http://dx.doi.org/10.1002/1097-0363(20010330)35:6<669::AID-FLD108>3.0.CO;2-#.

Hagen, S.C., Horstmann, O., Bennett, R.J., 2002. An unstructured mesh generation algorithm for shallow water modeling. Int. J. Comput. Fluid Dynam. 16 (2), 83–91. http://dx.doi.org/10.1080/10618560290017176.

Husain, S., Alavi, N., Bélair, S., Carrera, M., Zhang, S., Fortin, V., Abrahamowicz, M., Gauthier, N., 2016. The multi-budget soil, vegetation, and snow (SVS) scheme for improved land surface parameterization. Bangladesh J. Plant Taxon. 17, 137–141. http://dx.doi.org/10.1007/s13398-014-0173-7.2.

Imre, A.R., Novotný, J., 2016. Fractals and the Korcak-law: a history and a correction. Eur. Phys. J. H 41 (1), 69–91. http://dx.doi.org/10.1140/epjh/e2016-60039-8.

Ivanov, V., Vivoni, E., Bras, R., Entekhabi, D., 2004. Preserving high-resolution surface and rainfall data in operational-scale basin hydrology: a fully-distributed physically-based approach. J. Hydrol. 298 (1–4), 80–111. http://dx.doi.org/10.1016/j.jhydrol.2004.03.041.

John, V., 2000. A numerical study of a posteriori error estimators for convection–diffusion equations. Comput. Meth. Appl. Mech. Eng. 190, 757–781. http://dx.doi.org/10.1016/S0045-7825(99)00440-5.

Kumar, M., Duffy, C.J., Salvage, K.M., 2009a. A second-order accurate, finite volume–-based, integrated hydrologic modeling (FIHM) framework for simulation of surface and subsurface flow. Vadose Zone J. 8 (4), 873. http://dx.doi.org/10.2136/vzj2009.0014.

Kumar, M., Bhatt, G., Duffy, C.J., 2009b. An efficient domain decomposition framework for accurate representation of geodata in distributed hydrologic models. Int. J. Geogr. Inf. Sci. 23 (12), 1569–1596. http://dx.doi.org/10.1080/13658810802344143.

Lee, J., 1991. Comparison of existing methods for building triangular irregular net-work models of terrain from grid digital elevation models. Int. J. Geogr. Inf. Syst. 5 (3), 267–285.

Marsh, C.B., Pomeroy, J.W., Spiteri, R.J., 2012. Implications of mountain shading on calculating energy for snowmelt using unstructured triangular meshes. Hydrol. Process. 26 (12), 1767–1778. http://dx.doi.org/10.1002/hyp.9329.

McCartney, S.E., Carey, S.K., Pomeroy, J.W., 2006. Intra-basin variability of snowmelt water balance calculations in a subarctic catchment. Hydrol. Process. 20 (4), 1001–1016. http://dx.doi.org/10.1002/hyp.6125.

McGarigal, K., Marks, B.J., 1994. FRAGSTATS: Spatial Pattern Analysis Program for Quantifying LandscapesStructure. In: Gen. Tech. Rep. PNW-GTR-351 134 U.S. Dep. Agric. For. Serv. Pacific Northwest Res. Station, Portland, OR 97331(503).

Ménard, C.B., Essery, R., Pomeroy, J., Marsh, P., Clark, D.B., 2014. A shrub bending model to calculate the albedo of shrub-tundra. Hydrol. Process. 28 (2), 341–351. http://dx.doi.org/10.1002/hyp.9582.

Mott, R., Faure, F., Lehning, M., 2008. Simulation of seasonal snow-cover distribution for glacierized sites on Sonnblick, Austria, with the Alpine3D model. Ann. Glaciol. 49 (1), 155–160.

O'Callaghan, J.F., Marks, D., 1984. The extraction of drainage networks from digital elevation data. Comput. Vis. Graph Image Process 28 (3), 323–344.

Parrish, D.M., Hagen, S.C., 2007. 2D unstructured mesh generation for oceanic and coastal tidal models from a localized truncation error analysis with complex derivatives. Int. J. Comput. Fluid Dynam. 21 (7–8), 277–296. http://dx.doi.org/10.1080/10618560701582500.

Pomeroy, J.W., Schmidt, R.A., 1993. The use of fractal geometry in modelling intercepted snow accumulation and sublimation. In: 50th Annual Eastern Snow Conference, pp.

231–239 (Quebec City).

Pomeroy, J.W., Bewley, D.S., Essery, R.L.H., Hedstrom, N.R., Link, T., Granger, R.J., Sicart, J.E., Ellis, C.R., Janowicz, J.R., 2006. Shrub tundra snowmelt. Hydrol. Process. 20 (4), 923–941. http://dx.doi.org/10.1002/hyp.6124.

Pomeroy, J.W., Marsh, P., Gray, D.M., 1997. Application of a distributed blowing snow model to the Arctic. Hydrol. Process. 11 (11), 1451–1464.

Pomeroy, J.W., Parviainen, J., Hedstrom, N., Gray, D.M., 1998. Coupled modelling of forest snow interception and sublimation. Hydrol. Process. 12, 2317–2337.

Qu, Y., Duffy, C.J., 2007. A semidiscrete finite volume formulation for multiprocess watershed simulation. Water Resour. Res. 43 (8), 1–18. http://dx.doi.org/10.1029/2006WR005752.

Rineau, L., 2016. 2D conforming triangulations and meshes. In: CGAL User and Reference Manual, (CGAL Editorial Board).

Ruppert, J., 1995. A Delaunay refinement algorithm for quality 2-dimensional mesh generation. J. Algorithm 18 (3), 548–585. http://dx.doi.org/10.1006/jagm.1995.1021.

Shewchuk, J., 2002. Delaunay refinement algorithms for triangular mesh generation. Comput. Geom. 22 (1–3), 21–74. http://dx.doi.org/10.1016/S0925-7721(01)00047-5.

Shewchuk, J.R., 1996. Adaptive Precision Floating-Point Arithmetic and Fast Robust Geometric Predicates.

Shook, K.R., Gray, D.M., Pomeroy, J.W., 1993a. Geometry of patchy snowcovers. In: 50th Annual Eastern Snow Conference, pp. 89–98 (Quebec City).

Shook, K.R., Gray, D.M., Pomeroy, J.W., 1993b. Temporal variation in snowcover area during melt in prairie and alpine environments. Nord. Hydrol 24 (2–3), 183–198.

Tournois, J., Alliez, P., Devillers, O., 2010. 2D centroidal Voronoi tessellations with constraints. Numer. Math. J. Chin. Univ. 3 (2), 212–222. http://dx.doi.org/10.4208/nmtma.2010.32s.6.

VanDerWal, J., 2016. SDMTool.

Verfürth, R., 2005. Robust a posteriori error estimates for stationary convection-diffusion equations. SIAM J. Numer. Anal. 43 (4), 1766–1782. http://dx.doi.org/10.1137/040604261.

Vivoni, E.R., Ivanov, V.Y., Bras, R.L., Entekhabi, D., 2004. Generation of triangulated irregular networks based on hydrological similarity. J. Hydrol. Eng. 9 (August), 288.

Vrugt, J. a., ter Braak, C.J.F., Clark, M.P., Hyman, J.M., Robinson, B. a., 2008. Treatment of input uncertainty in hydrologic modeling: doing hydrology backward with Markov chain Monte Carlo simulation. Water Resour. Res. 44 (12). http://dx.doi.org/10.1029/2007WR006720.

Wulder, M. a., Nelson, T. a., 2003. EOSD Land Cover Classification Legend Report Version 2, Development. pp. 1–81.

Wulder, M.A., Cranny, M., Hall, R.J., Luther, J., Beaudoin, A., White, J.C., Goodenough, D.G., Dechka, J., 2007. Satellite land cover mapping of Canada's forests: the EOSD land cover project. In: North American Land Cover Summit, pp. 21–30.